

Article

Experimental Investigation and Mechanism Analysis on Rock Damage by High Voltage Spark Discharge in Water: Effect of Electrical Conductivity

Zhixiang Cai , Hui Zhang *, Kerou Liu, Yufei Chen and Qing Yu

College of Petroleum Engineering, China University of Petroleum-Beijing, 18 Fuxue Road, Changping, Beijing 102249, China; Zhixiang.cai05@gmail.com (Z.C.); liukerou1011@gmail.com (K.L.); yufeichen4323@gmail.com (Y.C.); yuqing1381@gmail.com (Q.Y.)

* Correspondence: zhanghuicup2018@163.com; Tel.: +86-132-6112-9527

Received: 23 September 2020; Accepted: 10 October 2020; Published: 18 October 2020



Abstract: High voltage spark discharge (HVSD) could generate strong pressure waves that can be combined with a rotary drill bit to improve the penetration rate in unconventional oil and gas drilling. However, there has been little investigation of the effect of electrical conductivity on rock damage and the fragmentation mechanism caused by HVSD. Therefore, we conducted experiments to destroy cement mortar, a rock-like material, in water with five conductivity levels, from 0.5 mS/cm to 20 mS/cm. We measured the discharge parameters, such as breakdown voltage, breakdown delay time, and electrical energy loss, and investigated the damage mechanism from stress waves propagation using X-ray computed tomography. Our study then analyzed the influence of conductivity on the surface damage of the sample by the pore size distribution and the cumulative pore area, as well as studied the dependence of internal damage on conductivity by through-transmission ultrasonic inspection technique. The results indicated that the increase in electrical conductivity decreased the breakdown voltage and breakdown delay time and increased the energy loss, which led to a reduction in the magnitude of the pressure wave and, ultimately, reduced the sample damage. It is worth mentioning that the relationship between the sample damage and electrical conductivity is non-linear, showing a two-stage pattern. The findings suggest that stress waves induced by the pressure waves play a significant role in sample damage where pores and two types of tensile cracks are the main failure features. Compressive stresses close horizontal cracks inside the sample and propagate vertical cracks, forming the tensile cracks-I. Tensile stresses generated at the sample–water interface due to the reflection of stress waves produce the tensile cracks-II. Our study is the first to investigate the relationship between rock damage and electrical conductivity, providing insights to guide the design of drilling tools based on HVSD.

Keywords: high voltage spark discharge; electrohydraulic effect; electrical conductivity; drilling; rock damage; pressure waves

1. Introduction

Improving the rate of penetration (ROP) is the focus of research in petroleum industries, because ROP is inversely proportional to drilling cost in unconventional reservoirs, which is typically 30% to 40% of the total well costs. Drilling at great depth is challenging, due to the hostile environment and the enhanced mechanical properties of the rock, making conventional rotary drilling methods inadequate. Over the past few decades, researchers and engineers have proposed some unconventional drilling techniques based on a different rock damage mechanism rather than using the drill bit's mechanical force to cut the rock. Laser drilling applies a continuous high-power laser beam to remove

the rock; researchers in the Gas Technology Institute have determined its technical feasibility and investigated the effects of specific laser energy on various rock types [1–3]. Electrical plasma drilling uses high thermal loads at thousands of degrees Celsius to spall, melt, and vaporize rock, where the thermal conductivity of the rock is a critical factor in breaking the rock [4,5]. However, lasers and plasma can generate high temperatures in downhole, disabling sensors near the drill bit that measure drilling parameters and formation characteristics, which are essential for directional drilling and risk analysis [6,7].

High voltage spark discharge (HVSD) can generate strong pulse pressure waves in water, known as the electrohydraulic effect (EHD) [8]. It has been adopted in a wide range of applications, such as underwater sound source, extracorporeal shock wave lithotripsy, well cleaning [9–11], and alternative hydraulic fracturing [12–16]. We have recently proposed a new drilling technology that couples the pressure waves of HVSD with the drill bit's mechanical force, which can potentially crush hard rock and increase the ROP without generating high temperatures like other new drilling techniques [17]. We conducted a series of laboratory experiments using pressure waves to destroy shale, sandstone, and concrete, and investigated the effects of discharge voltage, discharge energy, and the number of discharges on rock damage [18].

We have conceptually designed a new drilling system inspired by conventional rotary drilling (Figure 1). In this system, the drill string is connected to a custom drill bit with several HVSD reactors integrated into the bit's nozzle, and the power required to generate the electrohydraulic effect comes from either surface power supply or a downhole electric generator [19,20]. During drilling operations, the HVSD reactors create pressure waves amplified by ellipsoidal reflectors that act upon the rock. The rock is crushed to a depth of only a few millimeters, but this dramatically reduces the mechanical properties of the surface material, making it easier to be crushed by the drill bit, and increasing the ROP in hard rock and abrasive formations.

Numerous previous experiments employing HVSD to crush rocks used tap water with very low conductivity as the reaction medium, ignoring the effect of conductivity on pressure waves. However, in drilling practice, drilling fluids are complex compositional mixtures with a wide range of conductivities. Conductivity can influence the characteristics of high-voltage spark discharges, such as breakdown voltage, energy loss, and breakdown delay time, but previous studies have been inconsistent on the effect of conductivity on pressure wave intensity [21,22]. Moreover, few studies have been done on the effect of conductivity on HVSD fragmentation and the potential mechanism of rock breaking.

This research aims to investigate the effect of electrical conductivity on the discharge characteristics of high voltage spark discharge, the magnitude of pressure waves and rock damage, and to analyze the fragmentation mechanism from stress wave propagation. Then, we performed breaking experiments on cement mortar, an analogue for natural rock, with a single pulse energy of 1444 J in water with various conductivities. Utilizing mortar rather than natural rock is because the controllability and consistency of the mortar properties facilitate quantitative analysis of the relationship between conductivity and sample breaking. We reconstructed the model of the mortar sample before and after damage using X-ray computed tomography to analyze the damage mechanism, measured the surface damage by the size distribution and cumulative area of the pores, applied through transmission technique to detect microcracks inside the sample, and quantified the internal damage by the acoustic amplitude attenuation coefficient.

The results indicate that an increase in conductivity led to a nonlinear decrease in breakdown voltage, breakdown delay time, and an increase in energy loss. Both surface and internal damage of the samples exhibited a typical two-stage pattern, with pores and two types of tensile cracks being the predominant forms of damage. Stress waves induced by pressure waves propagating inside the sample play a crucial role, and tensile waves formed by reflection at the edge of the sample are among the leading causes of sample damage. The study offers some critical insights into the effect of electrical

conductivity on sample damage, which will provide significant guidance for drilling tools design, and facilitate the implementation of the drilling technology based on HVSD.

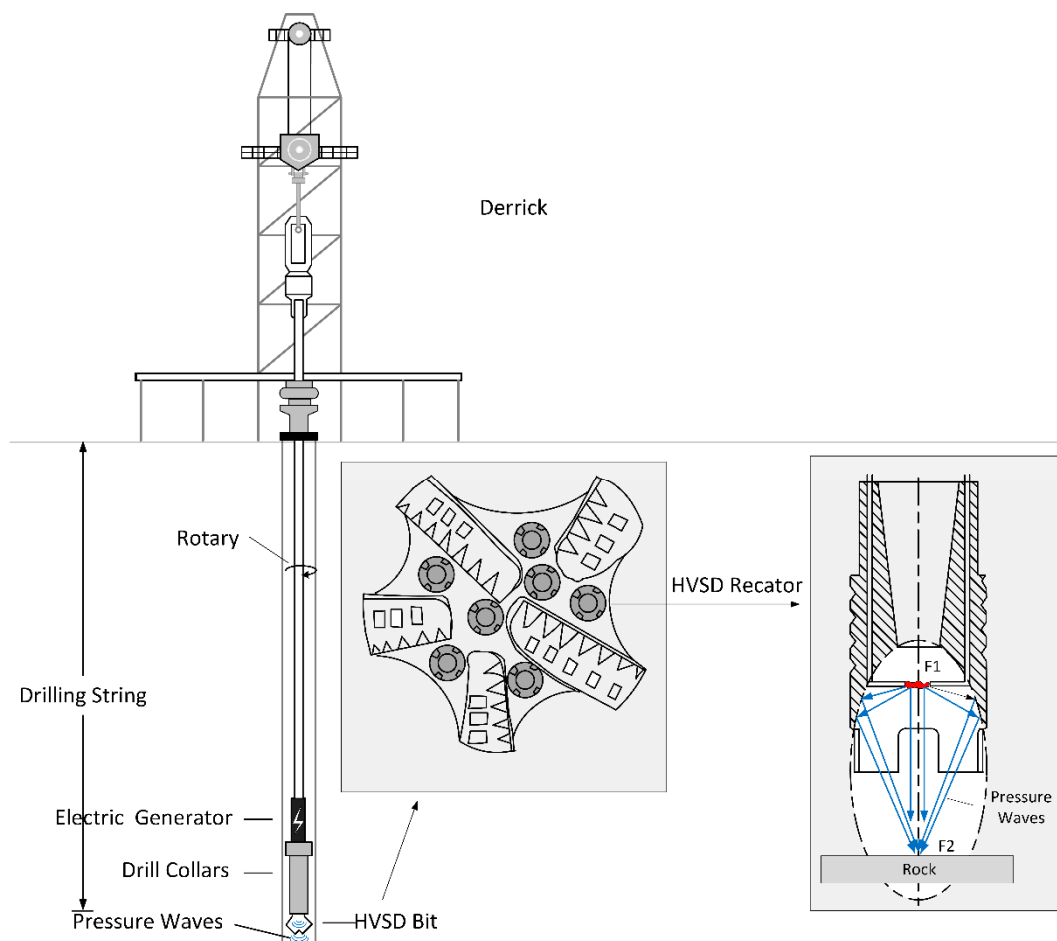


Figure 1. Conceptual design of drilling system based on the high voltage spark discharge.

2. Experiment

2.1. Sample Preparation

The absolute mass ratio of water, ordinary 42.5R Portland cement, and sand for pouring mortar was 0.5:1:1.8. The mechanical properties of the samples after 28 days of curing in water are shown in Table 1. Cubic samples of 100 mm in length, 100 mm in width, and 50 mm in height were prepared, from which some cylindrical samples of 25 mm in diameter and 30 mm in thickness were cut out (Figure 2). Mortar, like natural rocks, is a brittle material, and is often used in rock-breaking experiments, so the rock-breaking mechanism obtained from mortar is also applicable to natural rocks [13,23]. Since the mechanical properties of mortar samples from the same batch are almost identical, whereas the properties of natural rocks vary greatly, we used mortar to quantitatively study the effect of conductivity on rock damage.

Table 1. Mechanical properties of the mortar sample.

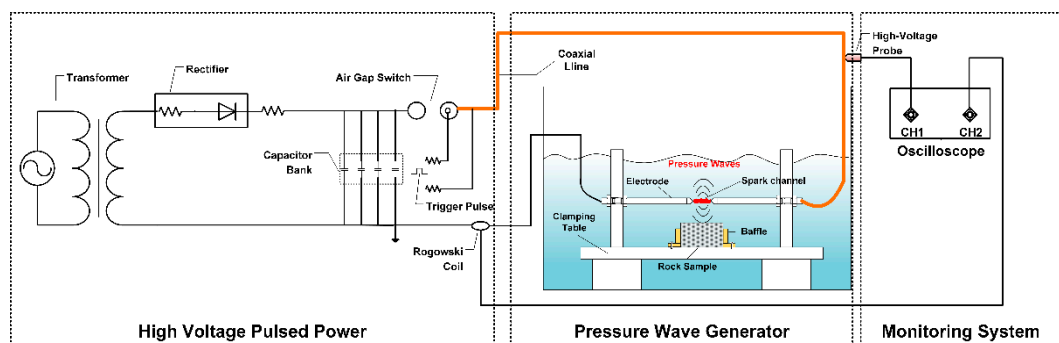
Sample	Density (g/cm ³)	Sound Velocity (m/s)	Acoustic Impedance (g/m ² s)	Compressive Strength (MPa)	Tensile Strength (MPa)	Elastic Modulus (MPa)
Mortar	2.44	4000	9.76×10^6	42	3.5	14,950



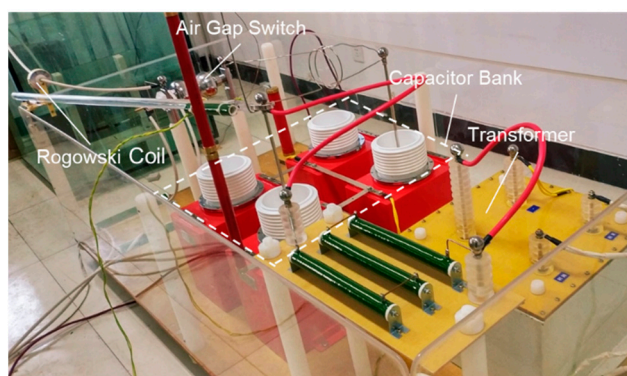
Figure 2. Two types of concrete sample.

2.2. Experimental Procedure

Experiments were conducted with high voltage discharge equipment, which consisted of a high voltage pulse power supply, a pressure wave generator, and a monitoring system. Figure 3a–c shows the diagram of the experimental equipment, the pulsed power supply components, and the pressure wave generator, respectively.



(a) Diagram of the experimental system



(b) High voltage pulsed power supply



(c) Pressure wave generator

Figure 3. High voltage spark discharge equipment.

The power supply mainly comprised a transformer, a rectifier, a high voltage capacitor bank, and an air-gap switch. When the power supply worked, the transformer raised the 220 V alternating current (AC) to a maximum of 70 kV, and then the rectifier converted the AC into the direct current (DC) to fully charge the capacitor bank. When the air-gap switch was closed, the energy stored on the

capacitor was released into the pressure wave generator through high-voltage coaxial cables, creating strong pressure waves from the electrohydraulic effect.

The capacitor bank contained four nominally 0.5 μF capacitors in parallel, providing operating pulse energy from 50 J/pulse up to 4.9 kJ/pulse. The pressure wave generator consisted of a cubic tank with 80 cm sides filled with water of varying conductivity, a pair of electrodes, and a sample clamping table. The electrodes were made of stainless steel with a tapered tip, 17 cm long and 1.5 cm in diameter. The sample was placed on the clamping table and confined by a baffle to prevent it from being moved by pressure waves. The gap between electrodes and the distance between the sample surface and the electrodes were then adjusted to 5 mm. Water with different conductivities was filled in the pressure wave generator until the electrodes were completely submerged.

Next, the pulse power was turned on to increase the voltage across the capacitor bank to a preset value. Once the capacitor bank was fully charged, the air-gap switch was closed to provide electrical energy to the electrodes.

A strong electric field was built up between the electrodes to break down the water and form a spark channel, bridging the electrodes under the Joule heating effect (Figure 3a). The temperature and pressure in the plasma-filled channel rise dramatically in a short time (about tens of microseconds), pushing the water around the channel and radiating pressure waves. The magnitude of the pressure waves can reach several hundred MPa, and can destroy rocks with a wide range of mechanical properties.

The voltage and current waveforms were measured by a high-voltage probe (Pintech P6039A) and a Rogowski coil, respectively, and recorded with an oscilloscope (Tektronix TPS2024B, the bandwidth of 200 MHz, and sample rates of 2 GS/s).

A charging voltage of 38 kV, a capacitance of 2 μF , single 158 pulse energy of 1444 J, and a discharge number of five were set. Five solutions with different conductivities of 0.5 mS/cm (tap water), 5 mS/cm, 10 mS/cm, 15,136 mS/cm, and 20 mS/cm were prepared by mixing tap water and NaCl (99.5% purity). Three mortar samples were used for each type of water with different conductivity.

2.3. Analysis of Damage Characteristics

The X-ray computed tomography (CT, nanoVoxel3502E, and imaging resolution of $\geq 0.5 \mu\text{m}$) was applied to observe the microscopic features of cylindrical sample before and after damage, to understand the mechanism of rock damage caused by pressure waves. Our study used the number of pores, and the distribution of pore sizes on the sample surface, to quantify the effect of conductivity on the surface damage. The pores were approximated as two-dimensional circles. Those with a diameter of less than 1 mm were neglected because they were mostly air bubbles caused during the sample casting process.

Apart from surface damage, it is also necessary to study the internal damage of the sample. Microcracks, the main form of the internal damage, occurring inside the sample due to the impacts of pressure waves and the interaction of the mortar particles with the stress waves, will hinder the propagation of acoustic waves, thereby attenuating the acoustic wave amplitude.

The acoustic wave amplitude was measured by an ultrasonic flaw detector (OLYMPUS 5077PR) with the through-transmission ultrasonic inspection technique (Figure 4). A transmitter (transmitting waves) and a receiver (receiving waves) were attached to opposite sides of the sample that were not directly damaged by the pressure waves. The two transducers and the sample were coupled by the ultrasonic coupling agent to ensure the transmission efficiency of acoustic energy. The attenuation of the wave amplitude, A_c , can be written in the form

$$A_c = \frac{(A_0 - A_1)}{A_0} \times 100\% \quad (1)$$

where A_0 is the ultrasonic wave amplitude measured before the sample was impacted by the pressure wave and A_1 is the wave amplitude after the impact of pressure wave.

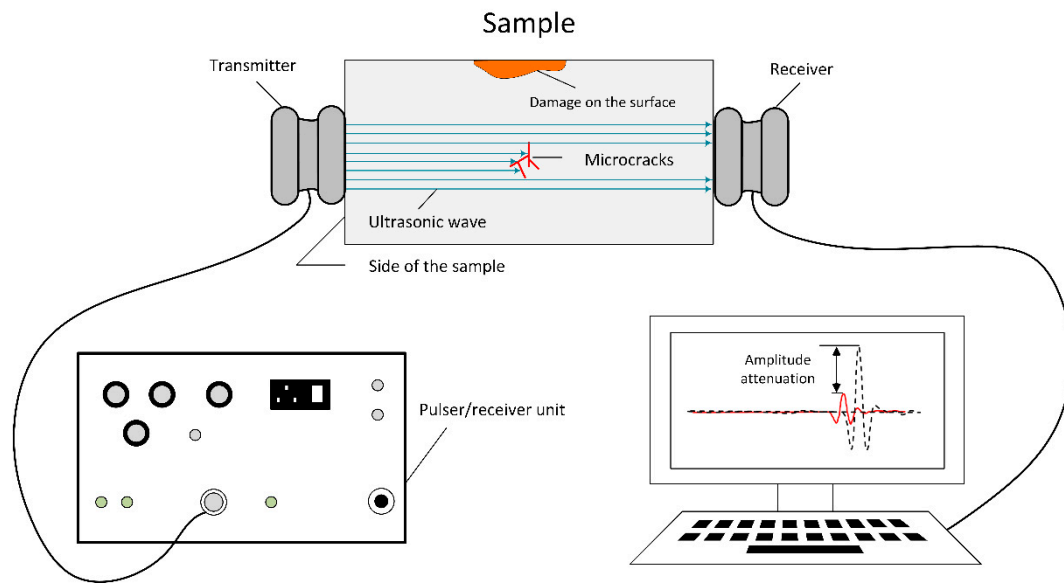


Figure 4. Schematic of ultrasonic transmission test.

3. Results and Discussion

3.1. Electrical Characteristics of Underwater Discharge at Different Conductivity

The voltage waveforms on the pair of electrodes were measured in water with different conductivity, and typical voltage waveforms are shown in Figure 5. The discharge voltage refers to the voltage on the positive electrode. The breakdown voltage is the voltage across the electrodes when the plasma channel is formed, and the time to breakdown is called breakdown delay time.

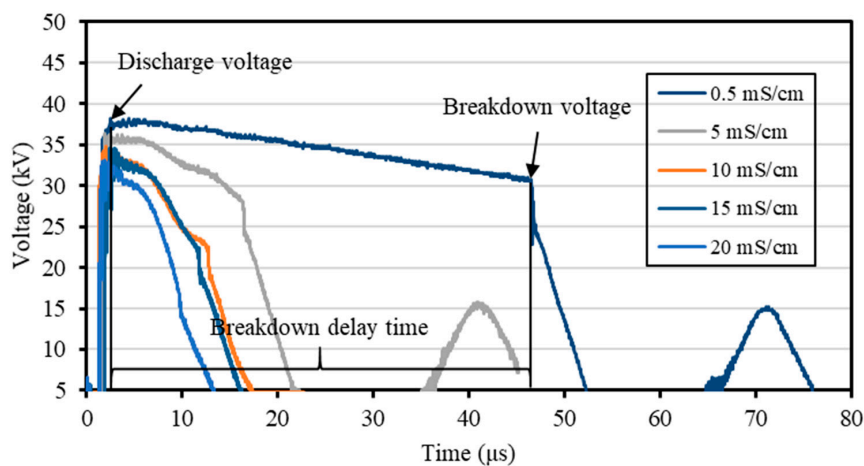


Figure 5. Voltage waveforms under the electrical conductivity from 0.5 mS/cm to 20 mS/cm.

Equation (2) expresses the efficiency of electrical energy in terms of the total energy stored in the capacitors, E_t (J), and the energy injected into the plasma channel, E_{pl} (J):

$$\eta = \frac{E_{pl}}{E_t} \times 100\% \quad (2)$$

where $E_t = \frac{1}{2} C V_d^2$, $E_{pl} = \frac{1}{2} C V_b^2$ (V_d is the discharge voltage, V_b is the breakdown voltage, and C is the capacitance of the capacitor bank).

Figure 6 shows the experimental data on the breakdown voltage under different electrical conductivity. Each value is an average of 15 replicates with a 95% confidence interval. As the electrical conductivity ranged from 0.5 mS/cm to 20 mS/cm, the breakdown voltage dropped from 31.1 kV to 14.8 kV. A similar result was also reported by Wang et al., where the breakdown voltage in 36 mS/cm KCL solution was lower than that in deionized water [24]. The mechanism of high voltage pulsed electrical breakdown in water indicates that the bubbles generated at the tip of the electrode are responsible for the breakdown of the water and the formation of the plasma channel [25–27]. In high-conductivity water, the electric field near the electrode tip produces a more intense field emission current, which will cause more water to evaporate and form more bubbles under the Joule heating effect, thus making electrical breakdown more likely to occur, which is manifested as a lower breakdown voltage on the voltage waveform.

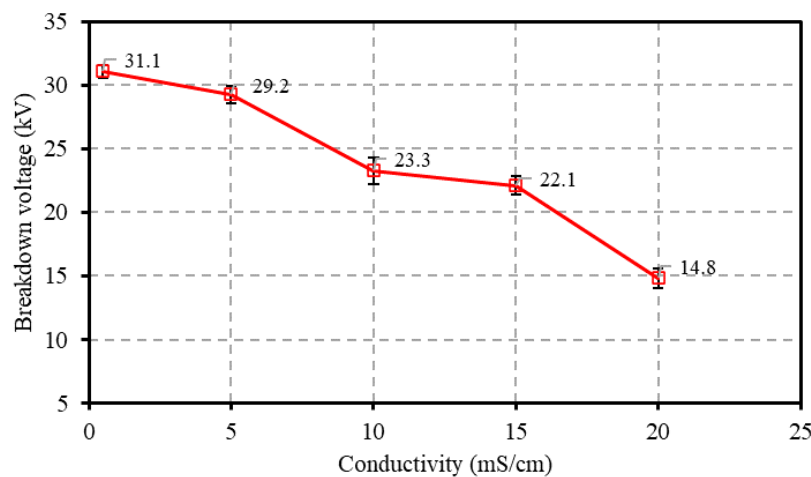


Figure 6. Breakdown voltage in water with different conductivity.

Figure 7 shows the relationship between breakdown delay time, t_b , and electrical conductivity. The most interesting aspect in this figure is that the t_b at 0.5 mS/cm is significantly larger than that of the other conductivities, while the value of t_b slightly decreases from 13 μ s to 10.2 μ s when the conductivity is increased from 5 mS/cm to 20 mS/cm. This result may be related to the Joule energy loss, E_{loss} (J), before water breakdown occurs, calculated by Equation (3)

$$E_{\text{loss}} = E_t - E_{\text{pl}} = \frac{1}{2}C(V_d^2 - V_b^2) \quad (3)$$

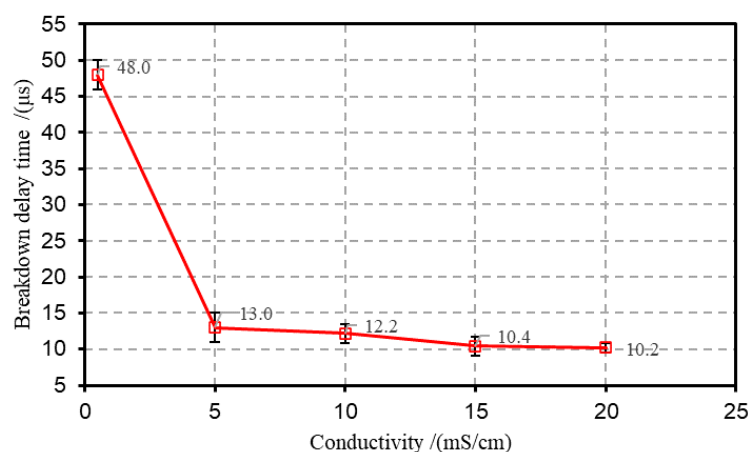


Figure 7. Breakdown delay time under different electrical conductivity.

Figure 8 shows that the electrical energy leaking into the water increases with increasing electrical conductivity. The major role of E_{loss} is to generate Joule heat in the water and form bubbles that contribute to the formation of electrical breakdown. Therefore, increasing the E_{loss} helps to reduce the breakdown delay time. When the conductivity is increased from 0.5 mS/cm to 5 mS/cm, E_{loss} increases by 71%, which explains the significant decrease in the breakdown delay time from 48 μs to 13 μs in this conductivity range (Figure 7).

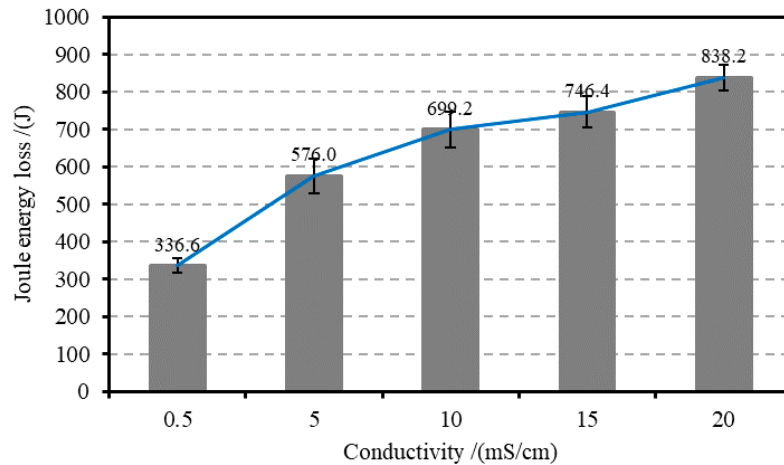
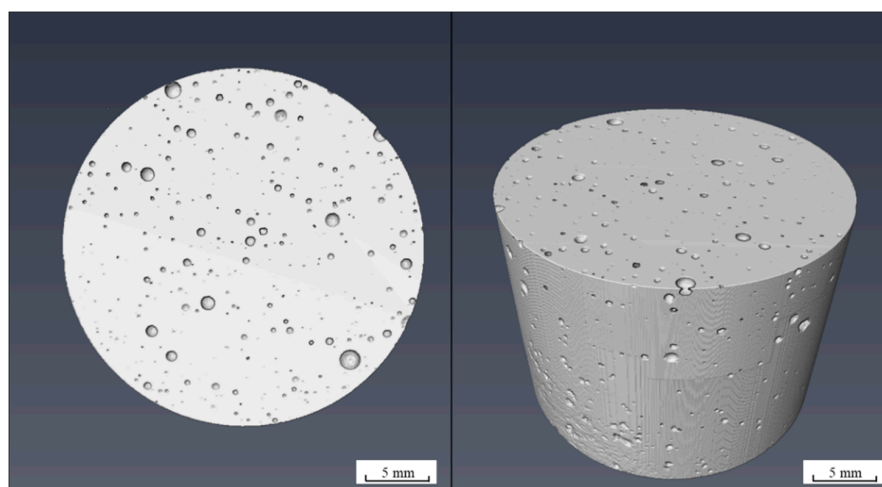


Figure 8. Joule energy loss under different electrical conductivity.

3.2. Damage of Samples under Different Electrical Conductivity

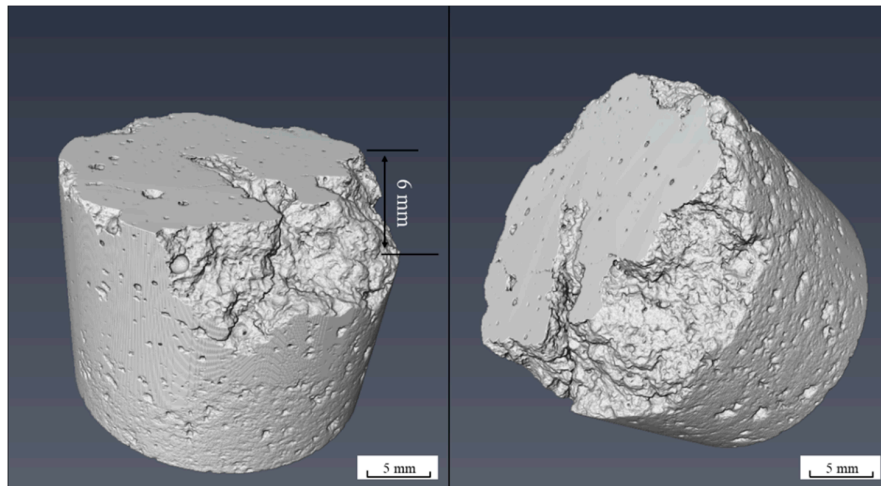
3.2.1. CT Results and Discussion

We applied the X-ray computed tomography (CT) to study the microscopic characteristics of a cylindrical sample with a diameter of 2.5 cm and a height of 3 cm. Figure 9 presents a sample model reconstructed by 3D visualization software before and after it was subjected to the pressure waves generated by underwater discharge. In Figure 9a, the pores (less than 1 mm in diameter) were air bubbles caused during the sample preparation process. As can be seen from Figure 9b, the sample was severely damaged after being hit by the pressure waves five times to a crushing depth of 6 mm, which significantly deteriorated the mechanical properties of the sample and made it easier to be crushed by the drill bit. Besides, some pits and cracks extended to the edge, causing the boundary of the sample to fall off.



(a) Sample morphology before the pressure waves

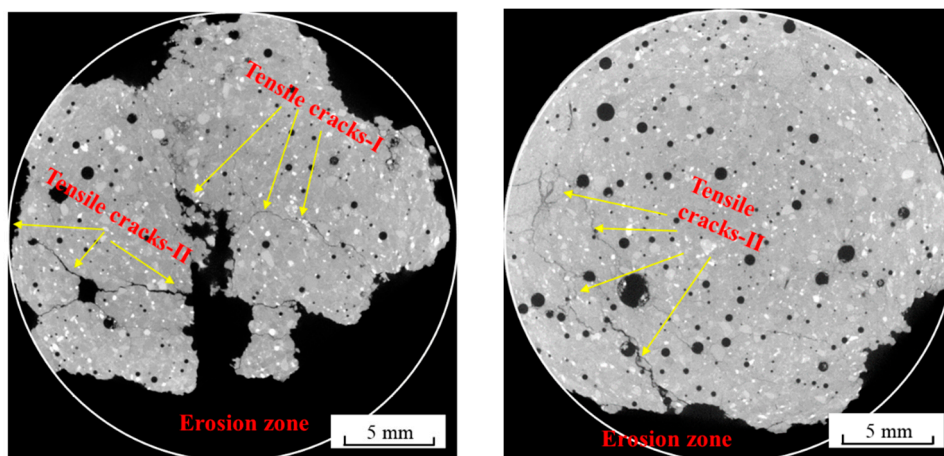
Figure 9. Cont.



(b) Sample morphology after the pressure waves

Figure 9. Three-dimensional reconstructed sample.

Figure 10 illustrates the sample surface's tomographic images and the images of 6 mm depth from the surface, respectively. It reveals that cracking and erosion are the main forms of damage caused by pressure waves. These results can be explained by the interaction between pressure waves and the mortar specimen (Figure 11a). A stress wave can be decomposed into a compressive stress wave and a shear stress wave. Rock samples often have pre-existing flaws, such as vertical cracks and horizontal cracks. When the sample is subjected to compressive stresses perpendicular to the sample surface, the horizontal cracks in the sample will close, and the vertical cracks will open and extend. According to the Inglis theory [28], stresses are concentrated and amplified at the tip of a vertical crack, and when the compressive stresses are higher than the strength at the crack tip, the crack grows parallel to the direction of compressive stresses. This type of crack refers to cracks-I in Figure 11a, common in uniaxial compression testing of brittle materials, and is also referred to as longitudinal splitting [29–31].



(a) Tomogram at the sample surface

(b) Tomogram at 6 mm from the surface

Figure 10. Tomographic images of the sample.

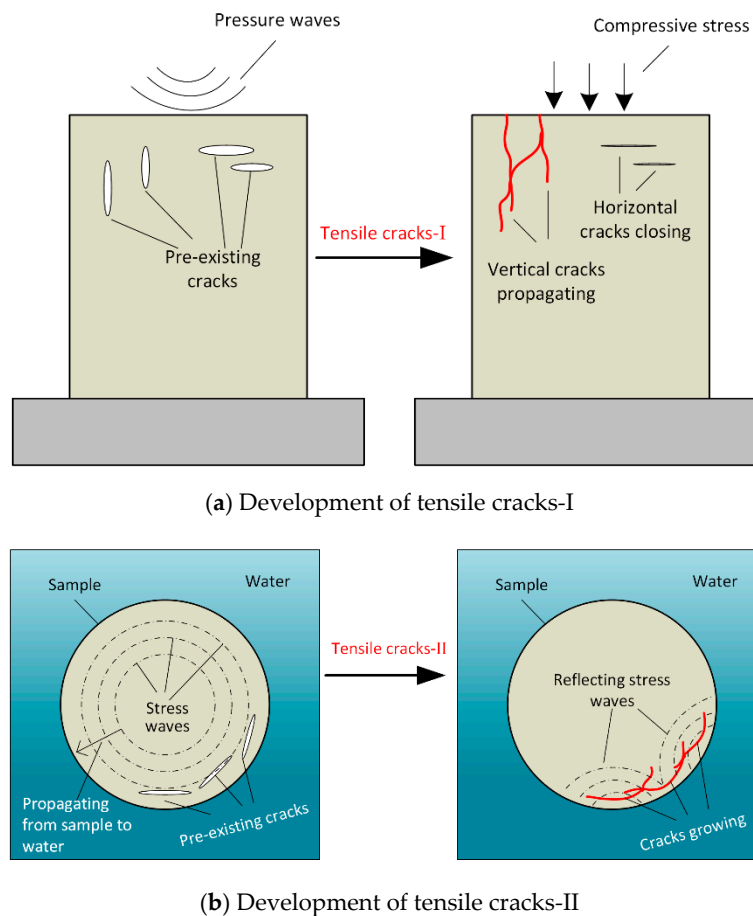


Figure 11. Schematic for the formation mechanism of tensile cracks-I and -II.

Tensile cracks-II, located at the edge of the sample, has a different formation mechanism than cracks-I. A stress wave propagates from the interior of the sample to the sample–water interface, where it is reflected and converted into a tensile wave, since the acoustic impedance of the sample is much higher than that of the water. This tensile stress causes tensile cracks if it exceeds the material’s tensile strength, known as spalling damage, and is typical of blast-induced damage and shock wave lithotripsy [32–34]. The cracks propagate further and interconnect with other cracks to form a continuous fault plane. When the stress exceeds the frictional resistance on the plane, frictional sliding and erosion will occur.

There were tensile cracks-I, tensile cracks-II, and extensive erosion of the sample surface (Figure 10a). As the depth increased, the damage degree decreased, and the damage was dominated by tensile cracks-II and erosion (Figure 10b).

3.2.2. Surface Damage Results and Discussion

Figure 12a shows the surface features of a raw sample, and Figure 12b–f show the typical surface macroscopic damage characteristics produced by pressure waves at different conductivities. The raw sample surface is smooth, while there are many cracks and pores on the surface of the samples crushed by the pressure waves. As the conductivity increased from 0.5 mS/cm to 20 mS/cm, the number of pores and the density of cracks gradually decreased.

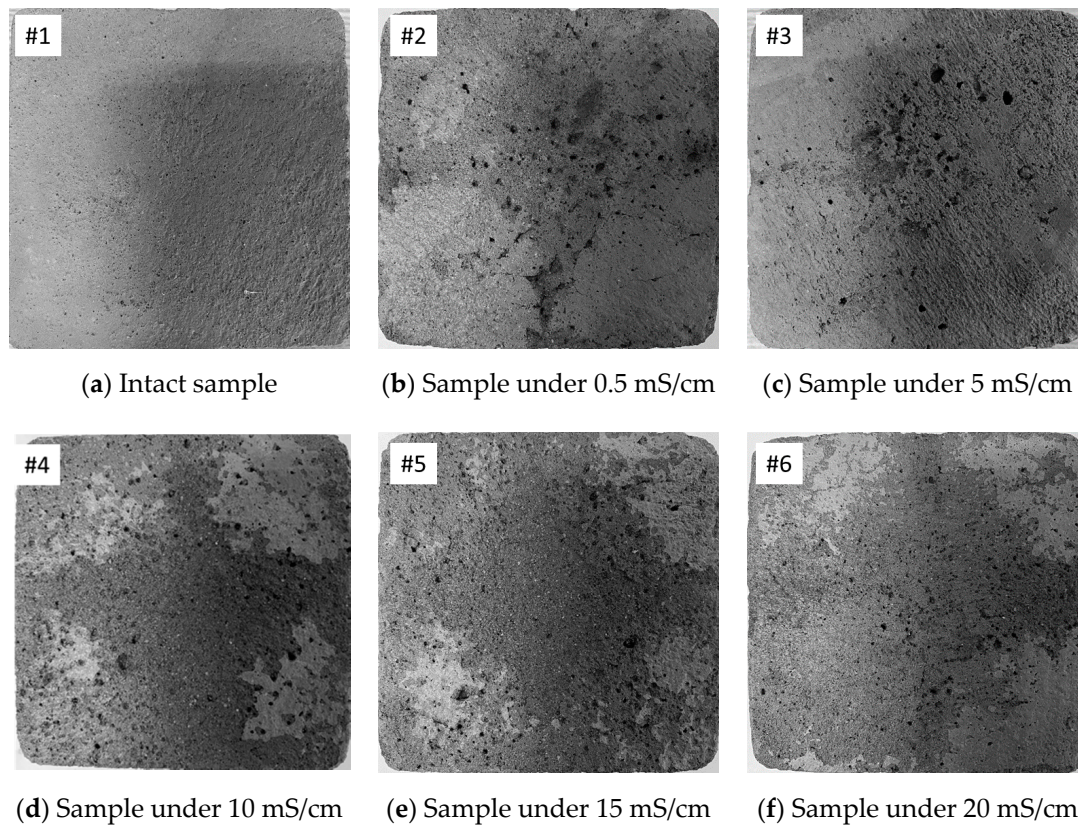


Figure 12. Typical surface macro-damage features of samples under different electrical conductivity.

We used the cumulative area of the pores, S , to quantitatively assess the effect of electrical conductivity on sample damage, with a higher S value indicating more significant damage. As shown in Figure 13, the value of S decreases significantly in water with high conductivity. For example, S at 20 mS/cm conductivity is only one-fifth of the value at 5 mS/cm. This result is related to the peak pressure of the pressure waves. The increase in conductivity leads to more energy leaking in the water, and less energy to form pressure waves, decreasing the peak pressure, P , and the S value (Figure 14). The P (MPa) is given in Equation (4) [35]:

$$P = 900 \frac{\left(\frac{E_{pl}}{1000} \right)^\alpha}{d} \quad (4)$$

where E_{pl} (J) is the electrical energy deposited into plasma channel, d (mm) is the distance between the channel and sample surface, and α denotes a coefficient, which is 0.35 in the experiment.

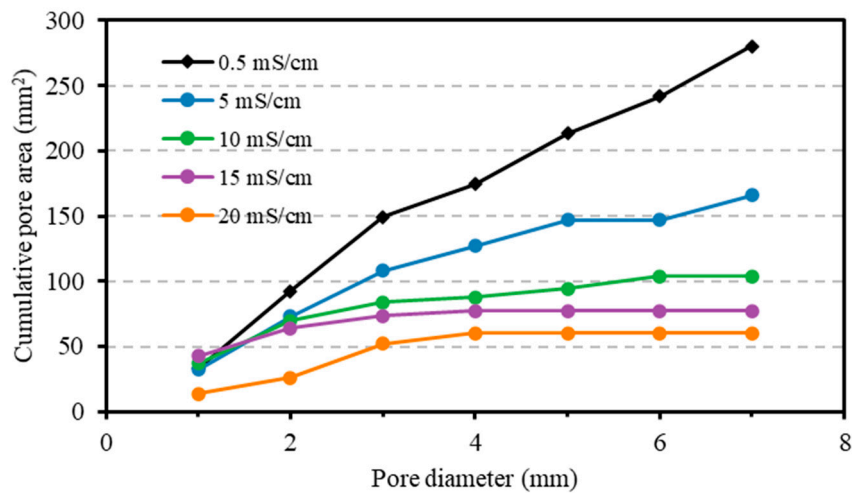


Figure 13. Cumulative pore area of samples broken by pressure waves.

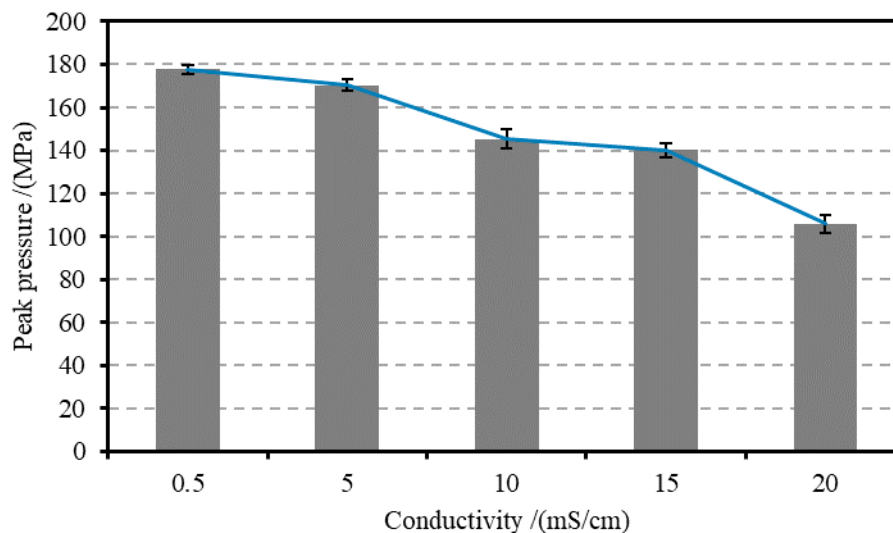


Figure 14. Peak pressure generated by electrical discharge under different conductivity.

Figure 15 illustrates the relationship between the average size distribution of pores on the sample surface and electrical conductivity. The pore size was dominated by 1 to 3 mm, and no pores larger than 6 mm in diameter were formed when the conductivity exceeded 10 mS/cm. Intuitively, the number of pores should be inversely proportional to the conductivity, but the number of pores with a 1 mm diameter increased first, and then decreased. One possible explanation is that in water with conductivities of 0.5 mS/cm and 5 mS/cm, many 1 mm pores are initiated early, but soon develop into larger dimensions because of the higher amplitude of the pressure waves (Figure 14). Therefore, in low conductivity, the number of 1 mm pores is fewer than that of relatively higher conductivity. However, when the conductivity is 20 mS/cm, the peak of pressure waves is considerably reduced by about 40%, resulting in a significant reduction in the number of pores of various sizes.

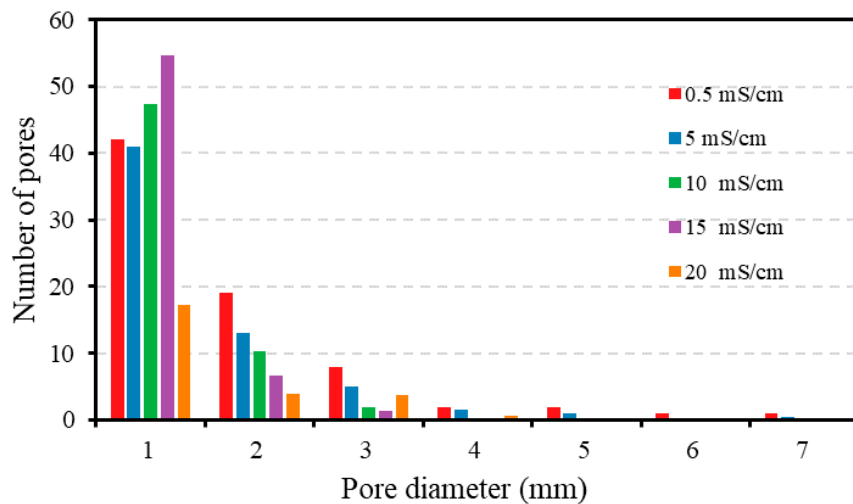


Figure 15. Number of pores on the sample surface under different electrical conductivity.

3.3. Internal Damage Results and Discussion

The through-transmission ultrasonic inspection technique allows the measurement of damage inside the sample, which is revealed in the reduced amplitude of received ultrasound waves, due to internal cracks and flaws that block the propagation of ultrasound waves.

Figure 16 shows the amplitude attenuation rate of samples, A_c , at different electrical conductivity. Each value is an average of three samples with 95% confidence interval precision. Interestingly, we found a two-stage pattern of internal damage. The A_c experienced a significant reduction from 61.1% at 0.5 mS/cm to 37.1% at 10 mS/cm, suggesting a rapid decrease in internal damage to the samples in this conductivity range. In contrast, there is little variation in A_c between 10 mS/cm and 20 mS/cm, indicating the number of flaws and microcracks within the samples are reducing, but at a slower rate. This two-stage pattern is also reflected in the sample surface damage (Figure 13), where the difference in surface damage between 0.5 mS/cm and 10 mS/cm is much more significant than the difference between 10 mS/cm and 20 mS/cm. The positive correlation between the internal and surface damages may suggest that pores and cracks on the surface grow downward under stress, creating new microcracks inside the sample, and deteriorating the mechanical properties of the sample. It seems that only when the stresses generated by the pressure wave are sufficiently higher than the compressive and tensile strengths, severe damage occurs.

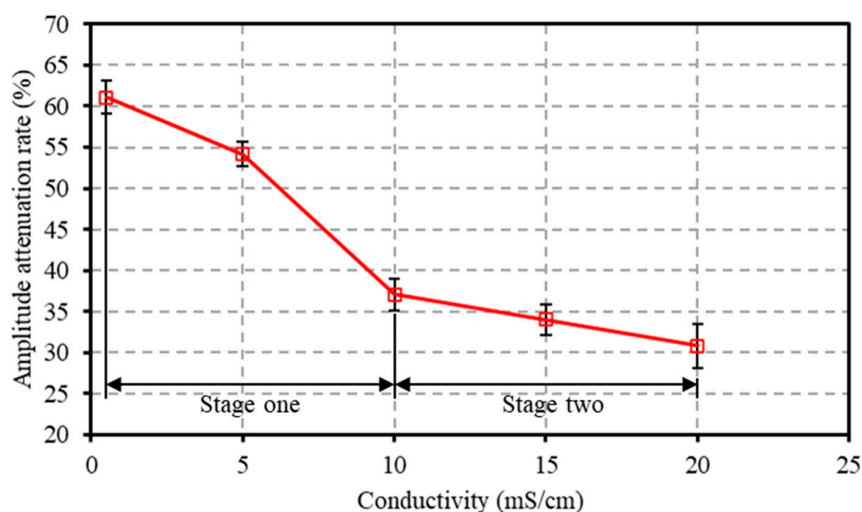


Figure 16. Amplitude attenuation rate under different conductivity.

4. Conclusions

This paper aims to investigate the characteristics of pulse discharge and the rock damage at different electrical conductivity, as well as the damage mechanism of pressure waves generated by HVSD.

Our study reveals that an increase in conductivity decreased the breakdown voltage and increased energy loss, thus decreasing the energy efficiency and the pressure wave's magnitude. However, the increase in conductivity reduces the difficulty and shortens the time required to form electrical breakdown, and accelerates the generation of pressure waves. As the conductivity increased from 0.5 mS/cm to 5 mS/cm, the breakdown delay time decreased rapidly, and remained almost constant as the conductivity increased. The sample damage exhibited a two-stage pattern in the range of 0.5 mS/cm to 20 mS/cm. Therefore, in practice, to balance energy efficiency, electrical breakdown time, and sample damage, the conductivity of water is preferably 5 mS/cm. The damage is mainly caused by pores and two types of tensile cracks, which are created by induced compressive stresses and tensile stresses induced by stress wave reflection at the mortar–water interface, respectively.

A limitation of this study is that we used the empirical formula from the literature [32] to calculate the peak pressure of the pressure wave, rather than measuring it experimentally. However, considering that our experimental system is the same as in the literature, the error in the peak pressure should be quite small. Besides, we neglected the effect of confining pressure and temperature on the damage process. In the future, we will establish an experimental system that can simulate the real stress state in the underground environment, and conduct HVSD rock-breaking tests at different temperatures and confining pressures to lay the foundation for the practical application of HVSD drilling technology in the oilfield.

Author Contributions: All the authors conceived and designed the study. Experiments: Z.C. and K.L.; data process: Z.C. and H.Z.; writing—original draft: Z.C. and H.Z.; writing—review and editing: Y.C., Q.Y., and K.L. All authors have read and agreed to the published version of the manuscript.

Funding: This research was funded by the National Natural Science Foundation of China (Grant No. 51774304, Grant No. 51734010, Grant No. U1762211, Grant No. 51574262, Grant No. 51774063, Grant No. U19B6003), National Oil and Gas Major Project (Grant No. 2017ZX05009), the Foundation for Innovative Research Groups of the National Natural Science Foundation of China (Grant No. 51821092), Strategic Cooperation Technology Projects of CNPC and CUPB (Grant No. ZLZX2020-01), Sinopec Joint Fund—Topic 5 (Grant No. U19B6003-5).

Acknowledgments: Thanks to Igor Timoshkin of the University of Strathclyde for his advice and help on the mechanism of underwater electrical discharge breakdown.

Conflicts of Interest: The authors declare that there is no conflict of interest regarding the publication of this paper.

References

- Xu, Z.; Reed, C.B.; Konercki, G.; Parker, R.A.; Gahan, B.C.; Batarseh, S.; Graves, R.M.; Figueroa, H.; Skinner, N. Specific energy for pulsed laser rock drilling. *J. Laser Appl.* **2003**, *15*, 25–30. [[CrossRef](#)]
- Sinha, P.; Gour, A. Laser Drilling Research and Application: An Update. In Proceedings of the SPE/IADC Indian Drilling Technology Conference and Exhibition, Mumbai, India, 16–18 October 2006; Society of Petroleum Engineers: Richardson, TX, USA, 2006.
- Salehi, I.A.; Gahan, B.C.; Batarseh, S. *Laser Drilling—Drilling with the Power of Light*; Institute of Gas Technology: Des Plaines, IL, USA, 2007.
- Gajdos, M.; Kocis, I.; Kristofic, T.; Horvath, G.; Jankovic, S. Utilization of Electrical Plasma for Hard Rock Drilling and Casing Milling. In Proceedings of the SPE/IADC Drilling Conference and Exhibition, London, UK, 17–19 March 2015.
- Gajdos, M.; Kristofic, T.; Jankovic, S.; Horvath, G.; Kocis, I. Use of Plasma-Based Tool for Plug and Abandonment. In Proceedings of the SPE Offshore Europe Conference and Exhibition, Aberdeen, UK, 8–11 September 2015; Society of Petroleum Engineers: Richardson, TX, USA, 2015.
- Gravley, W. Review of downhole measurement-while-drilling systems. *J. Pet. Technol.* **1983**, *35*, 1439–1445. [[CrossRef](#)]

7. Noureldin, A.; Irvine-Halliday, D.; Mintchev, M.P. Measurement-while-drilling surveying of highly inclined and horizontal well sections utilizing single-axis gyro sensing system. *Meas. Sci. Technol.* **2004**, *15*, 2426. [[CrossRef](#)]
8. Yutkin, L.A. Electrohydraulic Effect. Available online: https://scholar.google.com.hk/scholar?hl=zh-CN&as_sdt=0%2C5&q=+8.%09Yutkin%2C+L.A.+Electrohydraulic+Effect%3B+Air+Force+Systems+Command+Wright-Patterson+Afb+oh+Foreign+Technology+Division%2C+1961.&btnG= (accessed on 14 October 2020).
9. Chung, K.; Lee, S.; Hwang, Y.S.; Kim, C.Y. Modeling of pulsed spark discharge in water and its application to well cleaning. *Curr. Appl. Phys.* **2015**, *15*, 977–986. [[CrossRef](#)]
10. Bodykov, D.U.; Abdikarimov, M.S.; Seitzhanova, M.A.; Nazhipkyzy, M.; Mansurov, Z.A.; Kabdoldina, A.O.; Ualiyev, Z.R. Processing of Oil Sludge with the Use of the Electrohydraulic Effect. *J. Eng. Phys. Thermophys.* **2017**, *90*, 1096–1101. [[CrossRef](#)]
11. Xiong, L.; Liu, Y.; Yuan, W.; Huang, S.; Li, H.; Lin, F.; Pan, Y.; Ren, Y. Cyclic shock damage characteristics of electrohydraulic discharge shockwaves. *J. Phys. D* **2020**, *53*, 185502. [[CrossRef](#)]
12. Chen, W.; Maurel, O.; Borderie, C.L.; Reess, T.; Ferron, A.D.; Matallah, M.; Pijaudier-Cabot, G.; Jacques, A.; Rey-Bethbeder, F. Experimental and numerical study of shock wave propagation in water generated by pulsed arc electrohydraulic discharges. *Heat Mass Transf.* **2014**, *50*, 673–684. [[CrossRef](#)]
13. Chen, W.; La Borderie, C.; Maurel, O.; Pijaudier Cabot, G.; Rey Bethbeder, F. Simulation of damage–permeability coupling for mortar under dynamic loads. *Int. J. Numer. Anal. Methods Geomech.* **2014**, *38*, 457–474. [[CrossRef](#)]
14. Chen, W.; Maurel, O.; Reess, T.; De Ferron, A.S.; La Borderie, C.; Pijaudier-Cabot, G.; Rey-Bethbeder, F.; Jacques, A. Experimental study on an alternative oil stimulation technique for tight gas reservoirs based on dynamic shock waves generated by pulsed arc electrohydraulic discharges. *J. Pet. Sci. Eng.* **2012**, *88*, 67–74. [[CrossRef](#)]
15. Li, C.; Duan, L.; Tan, S.; Chikhotkin, V. Influences on high-voltage electro pulse boring in granite. *Energies* **2018**, *11*, 2461. [[CrossRef](#)]
16. Li, C.; Duan, L.; Tan, S.; Chikhotkin, V.; Fu, W. Damage model and numerical experiment of high-voltage electro pulse boring in granite. *Energies* **2019**, *12*, 727. [[CrossRef](#)]
17. Cai, Z.; Zhang, H.; Li, J.; Zheng, J.; Yu, Q.; Liu, K.; Liu, Y. New Technology to Assist Drilling to Improve Drilling Rate in Unconventional Gas Resources: Pulsed Arc Plasma Shockwave Technology. In Proceedings of the Abu Dhabi International Petroleum Exhibition & Conference, Abu Dhabi, UAE, 12–15 November 2018; Society of Petroleum Engineers: Richardson, TX, USA, 2018.
18. Cai, Z.; Zhang, H.; Li, J.; Yang, M.; Yu, Q.; Zheng, J.; Liu, K. An Experimental Study of Using Plasma Shock Wave for Rock Damage. In Proceedings of the Offshore Technology Conference, Houston, TX, USA, 6–9 May 2019.
19. Hui, Z.; Zhixiang, C. Well Drilling System and Method. CN108533172B, 28 May 2019.
20. Hui, Z.; Cai, Z. Plasma Generating Device, Fracturing System and Fracturing Method. CN111101915A, 5 May 2020.
21. Cathignol, D.; Mestas, J.L.; Gomez, F.; Lenz, P. Influence of water conductivity on the efficiency and the reproducibility of electrohydraulic shock wave generation. *Ultrasound Med. Biol.* **1991**, *17*, 819–828. [[CrossRef](#)]
22. Zhu, L.; He, Z.; Gao, Z.; Tan, F.; Yue, X.; Chang, J. Research on the influence of conductivity to pulsed arc electrohydraulic discharge in water. *J. Electrostat.* **2014**, *72*, 53–58. [[CrossRef](#)]
23. Yaşar, E.; Ranjith, P.G.; Viète, D.R. An experimental investigation into the drilling and physico-mechanical properties of a rock-like brittle material. *J. Pet. Sci. Eng.* **2011**, *76*, 185–193. [[CrossRef](#)]
24. Wang, H.; Wandell, R.J.; Tachibana, K.; Voráč, J.; Locke, B.R. The influence of liquid conductivity on electrical breakdown and hydrogen peroxide production in a nanosecond pulsed plasma discharge generated in a water-film plasma reactor. *J. Phys. D* **2018**, *52*, 75201. [[CrossRef](#)]
25. Marinov, I.; Guaitella, O.; Rousseau, A.; Starikovskaia, S.M. Modes of underwater discharge propagation in a series of nanosecond successive pulses. *J. Phys. D* **2013**, *46*, 464013. [[CrossRef](#)]
26. Fujita, H.; Kanazawa, S.; Ohtani, K.; Komiyama, A.; Kaneko, T.; Sato, T. Initiation process and propagation mechanism of positive streamer discharge in water. *J. Appl. Phys.* **2014**, *116*, 213301. [[CrossRef](#)]

27. Timoshkin, I.V.; Fouracre, R.A.; Given, M.J.; Macgregor, S.J. Hydrodynamic modeling of transient cavities in fluids generated by high voltage spark discharges. *J. Phys. D* **2006**, *39*, 4808. [[CrossRef](#)]
28. Inglis, C.E. Stresses in a Plate Due to the Presence of Cracks and Sharp Corners. *Trans. Inst. Naval Archit* **1913**, *55*, 219–241.
29. Fishman, Y.A. Features of compressive failure of brittle materials. *Int. J. Rock Mech. Min. Sci.* **2008**, *45*, 993–998. [[CrossRef](#)]
30. Han, L.; He, Y.; Zhang, H. Study of rock splitting failure based on griffith strength theory. *Int. J. Rock Mech. Min. Sci.* **2016**, *83*, 116–121. [[CrossRef](#)]
31. Wong, R.; Lin, P.; Tang, C.A. Experimental and numerical study on splitting failure of brittle solids containing single pore under uniaxial compression. *Mech. Mater* **2006**, *38*, 142–159. [[CrossRef](#)]
32. Wang, Z.; Li, Y.; Wang, J. Numerical analysis of blast-induced wave propagation and spalling damage in a rock plate. *Int. J. Rock Mech. Min. Sci.* **2008**, *45*, 600–608. [[CrossRef](#)]
33. Cleveland, R.O.; Sapozhnikov, O.A. Modeling elastic wave propagation in kidney stones with application to shock wave lithotripsy. *J. Acoust. Soc. Am.* **2005**, *118*, 2667–2676. [[CrossRef](#)] [[PubMed](#)]
34. Cao, S.; Zhang, Y.; Liao, D.; Zhong, P.; Wang, K.G. Shock-induced damage and dynamic fracture in cylindrical bodies submerged in liquid. *Int. J. Solids Struct.* **2019**, *169*, 55–71. [[CrossRef](#)]
35. Touya, G.; Reess, T.; Pécastaing, L.; Gibert, A.; Domens, P. Development of subsonic electrical discharges in water and measurements of the associated pressure waves. *J. Phys. D* **2006**, *39*, 5236. [[CrossRef](#)]

Publisher’s Note: MDPI stays neutral with regard to jurisdictional claims in published maps and institutional affiliations.



© 2020 by the authors. Licensee MDPI, Basel, Switzerland. This article is an open access article distributed under the terms and conditions of the Creative Commons Attribution (CC BY) license (<http://creativecommons.org/licenses/by/4.0/>).